

Spatial and temporal variation of hardness of a printed steel part

T. Mukherjee^a, T. DebRoy^{a,*}, T.J. Lienert^b, S.A. Maloy^c, P. Hosemann^d

^a Department of Materials Science and Engineering, The Pennsylvania State University, University Park, PA 16802, United States

^b Optomec, Inc. Albuquerque, NM 87109, United States

^c MST-8, Los Alamos National Laboratory, Los Alamos, NM 87545, United States

^d Department of Nuclear Engineering, University of California, Berkeley, CA 94704, United States



ARTICLE INFO

Article history:

Received 22 November 2020

Revised 26 January 2021

Accepted 21 February 2021

Available online 25 February 2021

Keywords:

3D printing

Additive manufacturing

Heat transfer and fluid flow

Martensite

Johnson-Mehl-Avrami

ABSTRACT

Several key industries routinely make complex parts using metal printing, but its continued growth will require the ability to control the microstructure and properties of parts. Many process variables affect the spatially variable thermal cycles that affect the microstructure and properties of parts. Here we show that the evolution of hardness of a tool steel part at various locations can be calculated using computed thermal cycles and a Johnson-Mehl-Avrami kinetic relation. The calculated hardness values agreed well with the independent experimental data for various processing conditions. At a given location, the hardness continued to decrease with progressive thermal cycles. Lower layers of the part experienced continued thermal cycles during the deposition of upper layers and the hardness decreased with distance from the top of the deposit. High heat input due to high laser power and slow scanning speed resulted in low cooling rate, high temperature, more pronounced tempering of martensite, and low hardness. Since the model can predict the spatial variation of hardness as a function of process variables, the work can serve as a basis for tailoring the hardness of some additively manufactured parts.

© 2021 Acta Materialia Inc. Published by Elsevier Ltd. All rights reserved.

1. Introduction

In directed energy deposition, unique three-dimensional metallic parts are now routinely made by melting and solidifying powder feedstock, layer upon layer, using a laser beam guided by a digital file [1–4]. The directed energy deposition (DED) additive manufacturing (AM) is widely used in aerospace, medical, and other industries [1,5,6]. An important challenge in this process is the need to control the microstructure and properties of metallic parts [2]. Although the process-microstructure-property-performance relations of metallic components have been extensively studied, there is no straightforward way to understand and control the evolution of the microstructures and properties of parts made by AM [1]. A large number of processing variables, the highly transient temperature fields, spatially variable thermal cycles, and the motion of the liquid alloys in the melt pool influence the solidification patterns, and the evolution of microstructure and properties of parts [1,2,4,7]. In addition, when a metal layer is deposited, the previously deposited layers are heated and cooled, and the microstructure and properties of the previously deposited layers

change [8–12]. Understanding the roles of process variables such as the laser power and scanning speed on the evolution of microstructure and properties are important because they affect the performance of the manufactured components.

Microstructure evolution has been studied in the allied process of fusion welding to investigate phase transformations in real-time using a powerful X-ray beam from synchrotron units [13]. These units provide crystal structure changes for the exact conditions of the experiment, but do not directly provide any data on the evolution of mechanical properties. Several attempts have been made to measure mechanical properties such as hardness and its spatial variations for parts made by DED-L [14–23]. Significant variations in hardness along the height of the printed parts due to a wide variety of microstructures in the component [14–23] have been reported. However, these results did not show the evolution of hardness during the deposition process. Several kinetic models [24–26] are available to explain the evolution of hardness by simulating the kinetics of martensite formation and its transformation to tempered martensite. For example, in the allied process of fusion welding of a dual phase steel, hardness variation has been predicted using a Johnson-Mehl-Avrami equation-based model which captures both the nucleation and growth mechanisms of carbides [27]. A martensite tempering kinetic model has been used to predict the hardness variation during multi-pass welding of a ferritic-martensitic steel [28]. In additive manufacturing, kinetic models

* Corresponding author.

E-mail address: debroy@psu.edu (T. DebRoy).

based on the Johnson-Mehl-Avrami equation [29,30] and particle coarsening models [31] have been used to explain the temporal evolution of hardness. These methods rely on the thermal cycles monitored experimentally during the AM process. However, experimental determination of thermal cycles at all locations in the part is not possible. In addition, the rapid movement of a tiny heat source to print the component makes the temperature measurement a difficult task [1,4]. A recourse is to do simulations where the complex thermal cycles are computed from the solution of the equations of conservation of energy, momentum, and mass [32–35] and the microstructural and property changes are computed from the computed thermal cycles. Such calculations require discretizing these equations and solving the resulting billions of equations in an iterative scheme and are computationally intensive [4]. Appropriate kinetic equations are needed to calculate microstructure evolution and changes in properties.

Here we use a combination of a well-tested, 3D, transient heat transfer and fluid flow model [5,36] and a kinetic model [30] to predict the hardness of H13 tool steel parts fabricated using multi-layer directed energy deposition with a laser heat source (DED-L). The heat transfer and fluid flow model is used to accurately calculate the thermal cycles at different locations of the component for various processing conditions. The effects of repeated heating and cooling are considered during the multi-layer deposition at all locations of the part as a function of time. The isothermal aging data of H13 tool steel [31] is used to calculate parameters of the phase transformation kinetic equation. The synthesis of the heat transfer fluid flow model, the phase transformation kinetics, and the isothermal aging data provide a framework for computing the effects of processing parameters on the microstructure and properties as a function of process variables that cannot be obtained by any other means. The calculated hardness values are rigorously tested using independent experimental data for various processing conditions. The model is also used to examine the effects of laser power and scanning speed on the hardness variations.

2. Methodology

Fig. 1 schematically represents the methodology used here. The hardness of a DED-L component is predicted by the following three consecutive steps. First, a well-tested, 3D heat transfer and fluid flow model [5,36] of DED-L is used to calculate accurate thermal cycles at specified locations. Second, the Johnson-Mehl-Avrami (JMA) equation gives the fraction of total martensite converted as a function of time for isothermal transformations. It has been shown in the literature that the change in hardness in a specimen is proportional to the fraction of transformation [37,38]. Therefore, in this case, hardness measurements from the specimens can be used to relate the phase transformation (tempering) kinetics to temperature and time, and the JMA parameters can be determined from the time-temperature-tempering data. Based on the isothermal aging data of H13 tool steel at various temperatures [31], constants in Johnson-Mehl-Avrami (JMA) equation are estimated. Finally, the isothermal JMA equation is integrated over the computed thermal cycle to calculate hardness. The various steps are explained in the following subsections.

2.1. Calculation of the thermal cycles

Thermal cycles are calculated using a well-tested, 3D, transient heat transfer and fluid flow model of DED-L of H13 tool steel. The model solves conservation equations of mass, momentum and energy in 3D to calculate the temperature and velocity fields, molten pool dimensions and multiple thermal cycles during the multi-layer deposition process at various selected locations in the part. The model is described in detail in our previous papers [5,36] and

Table 1

Thermo-physical properties of H13 tool steel used in thermal cycle calculations [39]. Here, 'T' represents temperature in K and ' γ ' is the surface tension.

Properties	Values
Liquidus temperature (K)	1725
Solidus temperature (K)	1585
Thermal conductivity (W/m K)	$18.39 + 7.52 \times 10^{-3}T$
Specific heat (J/kg K)	$394.8 + 0.2142T$
Liquid thermal conductivity (W/m K)	30.96
Liquid specific heat (J/kg K)	823.96
Latent heat of fusion (J/kg)	2.74×10^5
Density (kg/m ³)	7800
Viscosity (kg/m s)	5.7×10^{-3}
$d\gamma/dT$ (N/m K)	-0.43×10^{-3}

is not repeated here. Only the salient features of the model are presented here. Calculations are done for multi-layer thin walls. Cartesian coordinates are used in the calculation. Unidirectional laser scanning along the positive X-axis are used for all layers. The build direction of multiple layers follows the positive Z-coordinate. The direction perpendicular to the scanning direction along the width of the part is taken as the positive Y-direction. Half of the solution domain is used for the calculation to save computational time assuming symmetry with respect to vertical XZ plane. Thermal cycles are calculated at any location with a specified XYZ coordinate from the three-dimensional transient temperature field. Thermophysical properties of H13 tool steel [39] used for the calculations are presented in Table 1. Variations of the thermal conductivity and specific heat of the solid alloy with temperature are considered in the calculations. However, the effects of temperature on the thermophysical properties have been ignored where data are not available in the literature. It is also assumed that the thermophysical properties of the alloy are determined by the chemical composition and temperature. Possible effects of the microstructure of the alloy on the thermophysical properties at a given temperature are not known and ignored. These simplifying assumptions introduce inaccuracies in the calculations. However, the fair agreement between the experimentally determined thermal cycles and the corresponding computed results provide evidence that the computed thermal cycles can be used for the estimation of spatial and temporal variation of hardness.

2.2. Estimation of the constants in Johnson-Mehl-Avrami (JMA) equation

The JMA equation is used to estimate the extent of tempering of martensite as a function of time for isothermal transformations. It has been shown in the literature that the change in hardness in a specimen is proportional to the fraction of transformation [37,38]. Therefore, hardness measurements from the specimens can be used to relate the phase transformation (tempering) kinetics to temperature and time, and the JMA constants can be determined from the time-temperature-tempering data. The constants in JMA equation are estimated based on the isothermal aging data of H13 tool steel. Fig. 2(a) provides the isothermal aging data [31] which represents the hardness variation with aging time at different temperatures. As-deposited H13 martensitic tool steel parts exhibit high hardness [14,31]. Hardness decreases during aging because martensite transforms to tempered martensite containing carbides of vanadium and chromium [14,31] (Fig. 2(a)). A higher temperature can expedite tempering. Therefore, hardness decreases with aging temperature as shown in Fig. 2(a). Since, the change in hardness in a specimen is proportional to the fraction transformed [37,38,40], extent of tempering (Y) can be related to

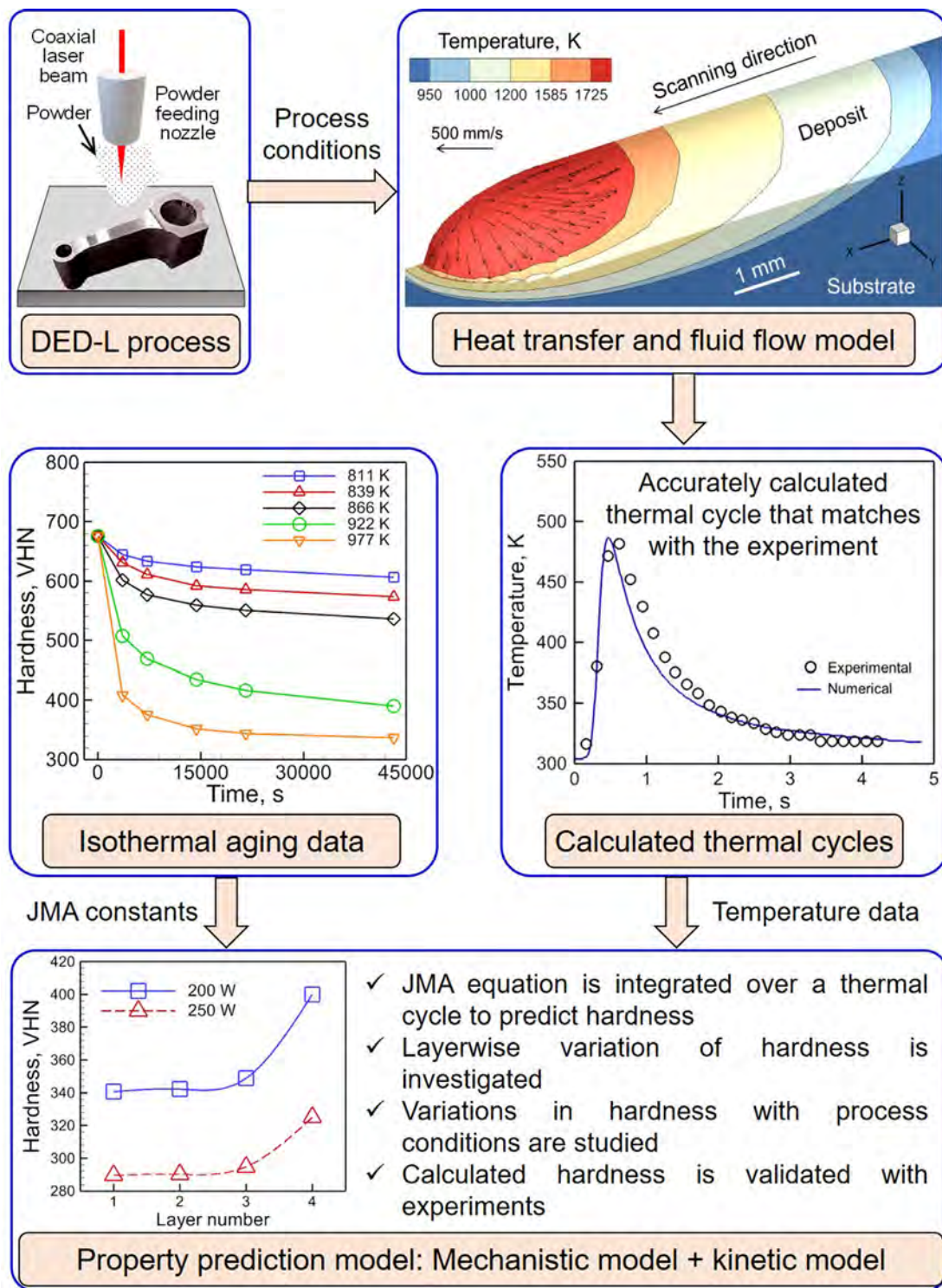


Fig. 1. This schematic outlines the method used in this research. The essential components are DED-L process, a mechanistic model (heat transfer and fluid flow) of DED-L process to compute thermal cycles and isothermal aging data for H13 tool steel to predict the constants in the John-Mehl-Avrami (JMA) equation. Both the mechanistic model and the JMA based kinetic model are combined to obtain a property prediction model to estimate hardness of H13 tool steel parts made using DED-L.

hardness (H) as,

$$Y = \frac{H_0 - H}{H_0 - H_\infty} \quad (1)$$

where $H_0 = 675$ VHN (maximum hardness in Fig. 2(a)), $H_\infty = 336$ VHN (minimum hardness in Fig. 2(a) after very long tempering) and H values at different time and temperature are obtained from the aging diagram (Fig. 2(a)). Variation of the extent of tempering

(Y) with time at different aging temperature is shown in Fig. 2(b). Extent of tempering (Y) can also be represented using JMA equation as [29,30],

$$Y = 1 - \exp[-k(t)^n] \quad (2)$$

where k and n are constants in JMA equation and t represents time in seconds. Therefore, slopes and Y -intercepts of Fig. 2(c) provide the values of n and $\ln(k)$ respectively, at different temperature,

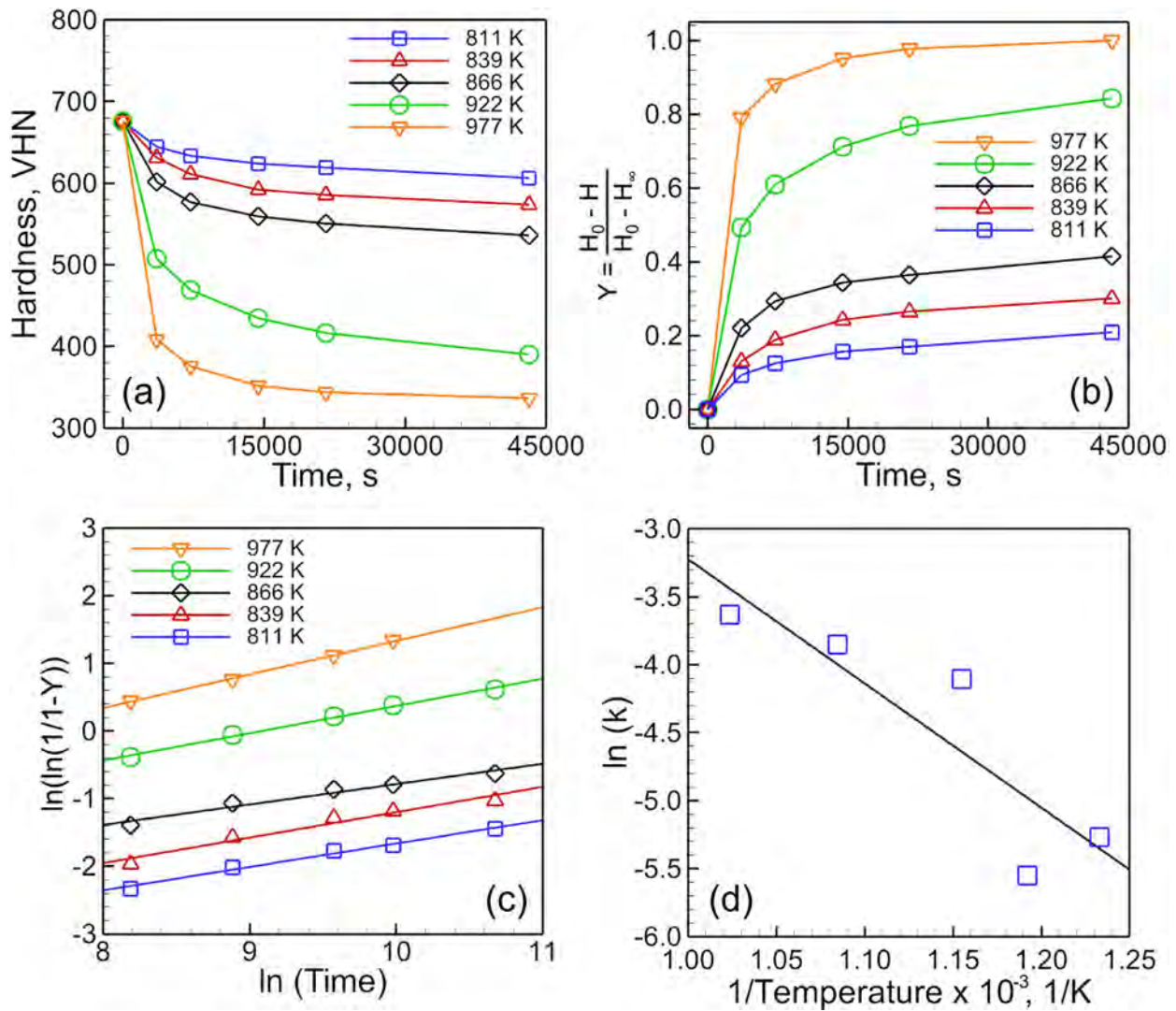


Fig. 2. Calculations of the constants in JMA equation for H13 tool steel. (a) Isothermal aging data [31] of H13 tool steel showing the variations in hardness with aging time at different temperature. (b) Calculated values of the extent of transformation (Y) with time at different temperatures. 'H' is the hardness taken from figure (a). H_0 and H_∞ are 675 and 336 VHN respectively. (c) Calculations of $\ln(k)$ and n in JMA equation. The y-intercept and slope of each line represent $\ln(k)$ and n respectively at the corresponding temperature. The values of $\ln(k)$ and n at different temperatures are provided in Table 2. The unit of 'k' is (seconds) $^{-0.41}$. (d) Plot of calculated values of $\ln(k)$ vs inverse of temperature. $\ln(k)$ values are taken from figure (c) at different temperatures. The slope of this plot provides the value of Q/R , where $Q = 7.593 \times 10^4$ J/mol and the y-intercept provides the value of $\ln(k_0) = 5.9$ (has same unit as $\ln(k)$) therefore, $k_0 = 367.8$. These values are used in the JMA equation.

Table 2

Data for calculating constants in JMA equations from the isothermal aging data of H13 tool steel. $\ln(k)$ and n are the y-intercepts and slope respectively, for different lines for different temperatures in Fig. 2(c).

Temperature, K	$\ln(k)$	n
811	-5.2689	0.36
839	-5.5515	0.44
866	-4.1062	0.34
922	-3.8523	0.42
977	-3.63	0.49
Average n		0.41

which are provided in Table 2. The constant k in Eq. (2) can be represented as [29,30],

$$k = k_0 \exp(-Q/RT) \quad (3)$$

Table 3

Process parameters used for the calculations.

Process parameters	Set 1	Set 2	Set 3
Laser power (W)	200–250	680	800
Laser scanning speed (mm/s)	8.47–10.58	12.7	2.0
Laser beam radius (mm)	0.45	0.50	0.53
Layer thickness (mm)	0.45	0.25	1.0
Powder feed rate (g/s)	0.217	0.22	0.22
Track length (mm)	8.0	35.5	45.0
Substrate thickness (mm)	1.5	9.0	5.0

where k_0 is an alloy specific constant, T is the temperature in K, Q is the activation energy in J/mol K and R is the universal gas constant (8.314 J/mol K). Slope of a plot of $\ln(k)$ with the inverse of temperature ($1/T$) (Fig. 2(d)) provides the value of Q/R , where $Q = 7.593 \times 10^4$ J/mol and Y-intercept provides the value of $\ln(k_0) = 5.9$ which gives $k_0 = 367.8$ (seconds) $^{-0.41}$. An average value of $n = 0.41$ is taken for the calculation (Table 2).

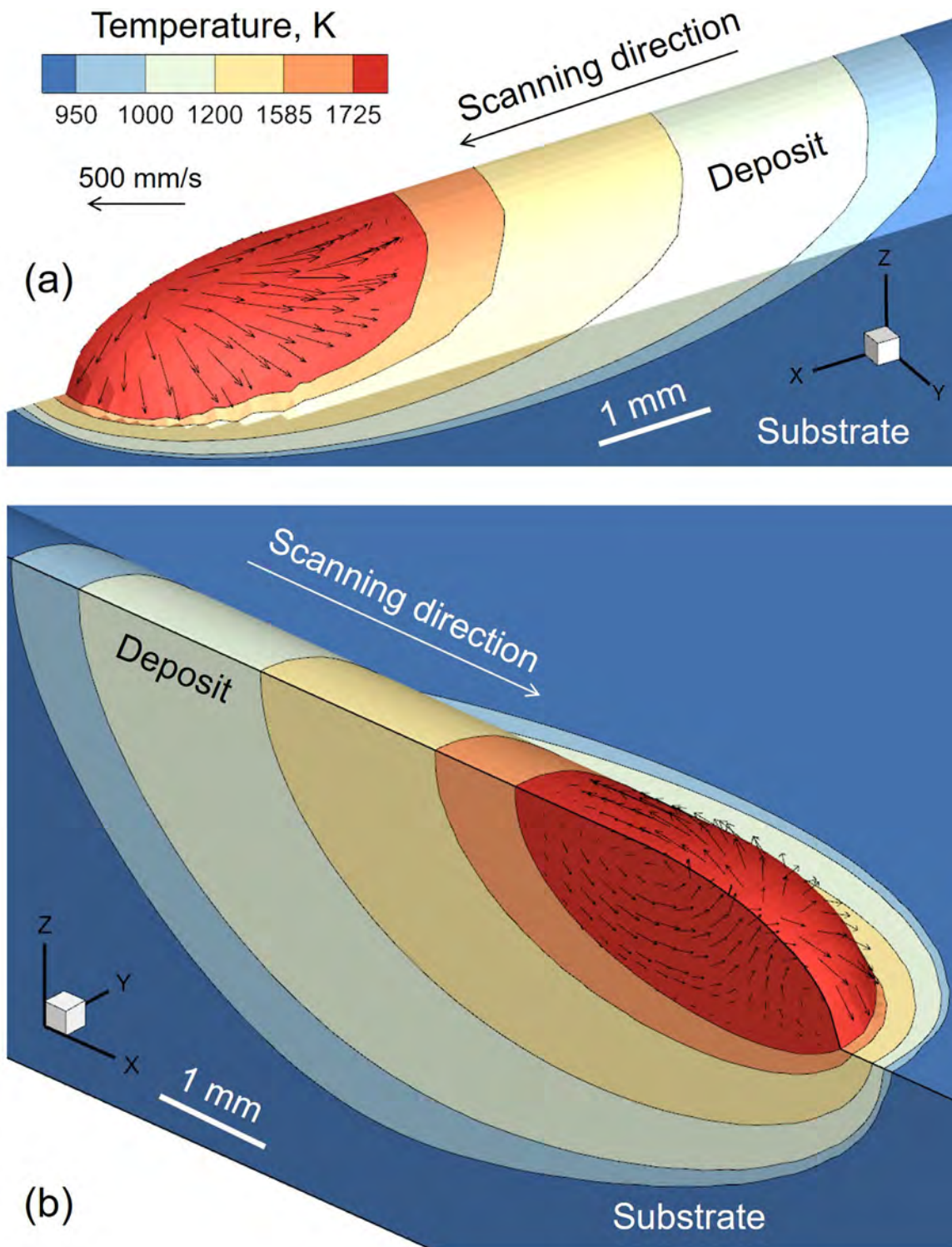


Fig. 3. 3D temperature and velocity fields in two isometric views (a) and (b), calculated using the heat transfer model for DED-L of H13 tool steel using 250 W laser power and 8.47 mm/s scanning speed. Other process parameters are given as set 1 in Table 3. Half of the domain is shown due to symmetry about XZ plane.

2.3. Predication of hardness from the thermal cycle

Hardness of the component is calculated by integrating the isothermal JMA equation (Section 2.2) over the numerically computed thermal cycles (Section 2.1). The thermal cycle is assumed to be a summation of multiple small isothermal time steps. At each time step, the time elapsed is a fraction of the time required,

at that temperature, to achieve a given amount of transformation or change in hardness. Summation of isothermal time steps (Δt), where Δt is in seconds, over an entire thermal cycle covers the overall aging process [31],

$$\sum \frac{\Delta t}{t} = 1 \quad (4)$$

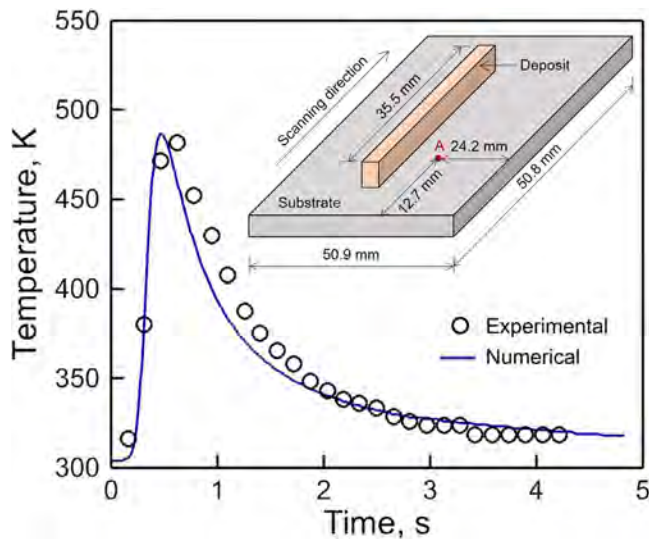


Fig. 4. Comparison between experimentally monitored [41] and numerically calculated thermal cycle during DED-L of H13 tool steel using the process parameters given as set 2 in Table 3. The thermal cycle is for a single layer deposition. Experimentally, the temperature is monitored using a thermocouple at a location 'A' schematically shown in the inset. The inset to show the process is a schematic and not to scale. The thermal cycle is numerically calculated at "A".

where t is time in seconds, can be found by combining Eq. (1) to (3) and rearranging the terms as,

$$t = \left[\frac{\ln\left(1 - \frac{H_0 - H}{H_0 - H_\infty}\right)}{-k_0 \exp\left(\frac{-Q}{RT}\right)} \right]^{1/n} \quad (5)$$

In Eq. (5), T is the temperature (in K) from the computed thermal cycle. The constants and their values are discussed in Section 2.2. For an isothermal hold, Eq. (5) represents the time required to reach a given hardness (H), at a given temperature (T). Eq. (4) is iteratively solved over a thermal cycle to find the value of the hardness (H) that satisfies the summation for that thermal cycle.

3. Results and discussion

Fig. 3 shows the three-dimensional temperature and velocity fields during DED-L of a single-track H13 tool steel deposit when the laser beam is at the mid length of the track. The red region bounded by the liquidus temperature isotherm (1725 K) represents the fusion zone of the molten pool. The liquidus (1725 K) and solidus (1585 K) temperature isotherms bound the two-phase solid-liquid mushy zone. Isotherms are compressed near the leading edge and expanded near the trailing edge of the molten pool due to scanning along the positive x -direction. In DED-L, the part is made by melting and solidification of powder particles. Therefore, the top surface of the deposit is curved, with the height at a maximum at the center and decreasing along the y -direction away from the center of the deposit, as shown in Figs. 3 (a-b). Black velocity vectors represent the convective flow of the liquid metal driven by the surface tension gradient on the top surface. The magnitude of these velocities can be estimated by comparing their length with that of the reference vector provided. The liquid metal flows from the center (low surface tension at high temperature) to the periphery (high surface tension at low temperature) of the molten pool along the curved top surface.

Thermal cycles at any location in the component can be extracted from the 3D, transient temperature distributions (Fig. 3). Fig. 4 shows that the calculated thermal cycle agrees well with the

experimentally measured values [41] for a single layer deposition of a H13 tool steel build for which data are available. The deposit fabricated on a substrate is schematically shown in the inset of the figure. The temperature was experimentally measured [41] using a thermocouple at a location indicated as 'A' in the figure. The thermal cycle is calculated at the same location. The excellent agreement between the experimental and numerical calculations indicates that the computed thermal cycles can be used for the calculations of hardness with confidence.

Accurate thermal cycles can be extracted at any location in the deposit from the numerically computed 3D, transient temperature fields. For example, Figs. 5 (a-d) show the temperature distributions on the longitudinal plane while depositing four layers based on which thermal cycle is calculated at a location 'A' in the first layer (Fig. 5(e)). During the deposition of the first layer, the location 'A' experiences the maximum temperature. As subsequent layers are deposited, the laser beam moves away from the location 'A' which reduces the temperature at that location. The peak temperature at location 'A' decreases as more layers are deposited (Fig. 5(e)). In addition, the location 'A' experiences repeated heating and cooling cycles during the deposition of four layers. The repeated heating and cooling affect the hardness at 'A' during the deposition process. For example, after the deposition of the first layer, the hardness at 'A' is very high (around 325 VHN in Fig. 5(f)) due to the formation of martensite. Martensite forms because the cooling rate (slope of the computed thermal cycle while depositing the first layer) at the martensite start temperature (around 590 K) [18] is about 300 K/s which is much above the critical cooling rate [18] of martensite formation (1 K/s) for H13 tool steel. Repeated heating and cooling during the deposition of subsequent layers transforms martensite to tempered martensite (increasing % of tempering in Fig. 5(f)) containing carbides rich in vanadium and chromium. The tempering decreases the hardness. Therefore, hardness at the location 'A' decreases with the deposition of the upper layers as shown in Fig. 5(f).

Fig. 5 explains the variation in hardness at a fixed location 'A' in the first layer during the deposition of four layers. Similarly, the variation in hardness can be calculated at any location at different layers. Fig. 6 and 7 explain the variation in hardness at four different locations 1, 2, 3 and 4 at first, second, third and fourth layers, respectively. Figs. 6 (a-d) show the temperature distribution on the longitudinal plane while depositing four layers from which the thermal cycles are calculated at the four locations. During the deposition of the first layer the location '1' experiences the maximum temperature. As subsequent layers are deposited the laser beam moves far from the location '1' which reduces the temperature at that location. Therefore, the peak temperature experienced by the location '1' decreases as more layers are deposited as shown in Fig. 6(e). Similarly, the locations indicated by 2, 3 and 4 experience maximum temperatures during the deposition of the 2nd, 3rd and 4th layers respectively. In addition, the thermal cycle at the location '1' shows that the location experiences multiple repeated heating and cooling as more layers are deposited. In total, this location experiences four heating and cooling cycles during the deposition of 1st to 4th layers as shown in Fig. 6(e). Similarly, the location '2' experiences three heating and cooling cycles during the deposition of 2nd to 4th layers. Location '3' and '4' experience two and one cycles, respectively (Fig. 6(e)). The repeated heating and cooling at each location affect their hardness variation during the deposition process (Fig. 7).

Calculated variations of hardness and percentage tempering of martensite at 4 layers (calculated at the four locations "1" to "4" shown in Fig. 6) during the depositions of 4 layers are shown in Fig. 7(a) and (b) respectively. Fig. 7(a) shows that after the deposition of the first layer, the location '1' exhibits a very high hardness (around 325 VHN) due to the formation of martensite (0% temper-

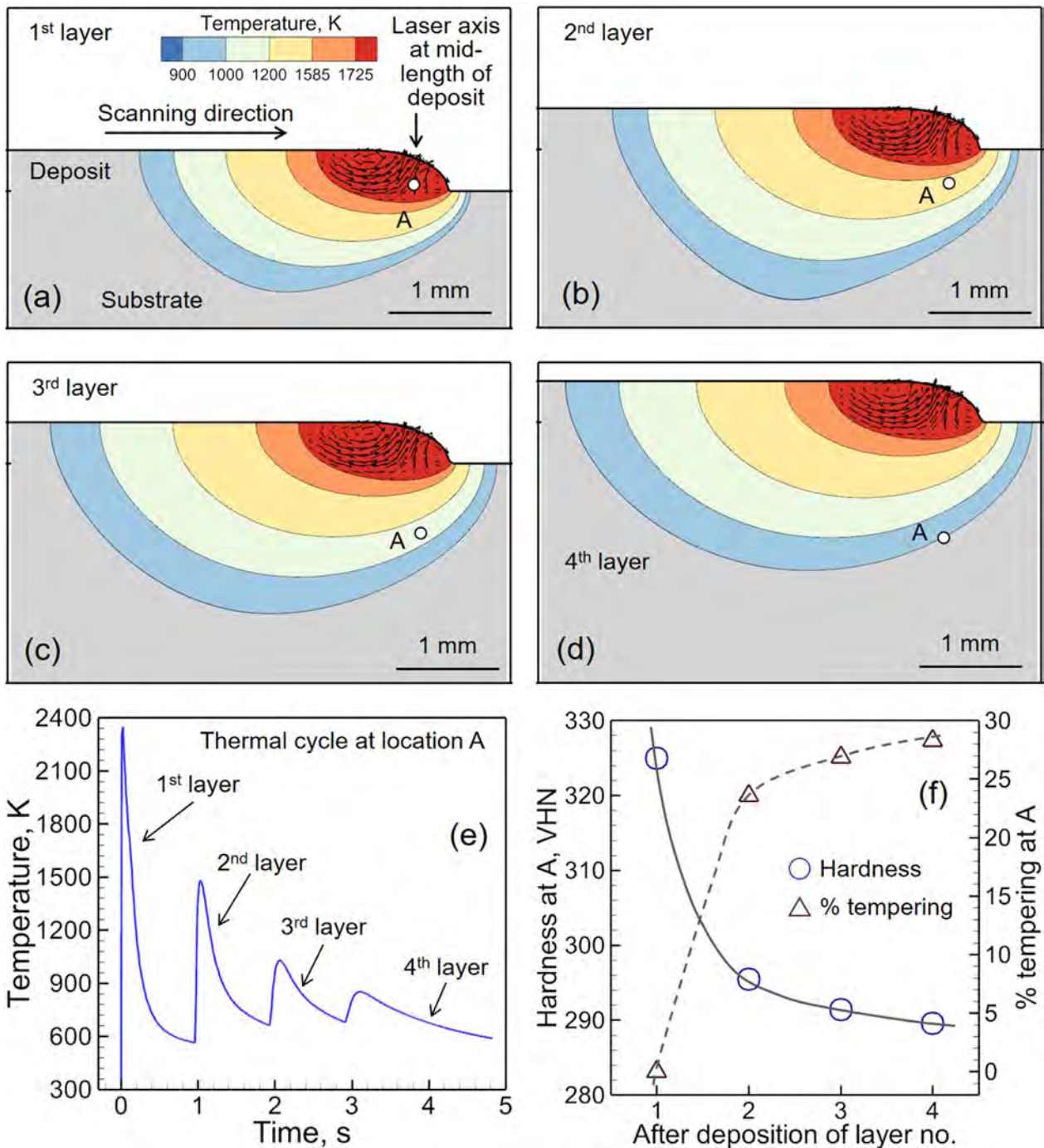


Fig. 5. Computed temperature and velocity fields on longitudinal plane (XZ as shown in Fig. 3) at the mid-width of the deposit during DED-L of H13 tool steel during the deposition of (a) 1st, (b) 2nd, (c) 3rd and (d) 4th layer. The results are for 250 W laser power and 8.47 mm/s scanning speed. Other process parameters are given as set 1 in Table 3. 'A' is a fixed location at the 1st layer as shown in the figures. (e) Thermal cycle calculated at the location 'A' while depositing the 4 layers. (f) Calculated variation in hardness and percentage tempering of martensite at location 'A' during the deposition of 4 layers.

ing in Fig. 7(b)). Similarly, very high hardness values are observed at locations 2 (layer 2), 3 (layer 3) and 4 (layer 4) after the deposition of the 2nd, 3rd and 4th layers respectively. Repeated heating and cooling during the deposition of subsequent layers temper martensite (Fig. 7(b)) which decreases hardness (Fig. 7(a)). Therefore, hardness decreases with the deposition of upper layers. Reduction in hardness is greater for a location that experiences a higher number of heating and cooling cycles. For example, the location '1' (in layer 1) exhibits the least hardness (Fig. 7(a)) after the deposition of the 4th layer since it experiences four thermal

cycles which results in the highest amount of tempered martensite (Fig. 7(b)). The hardness at location '2' after the deposition of the 4th layer is higher than that in location '1' because location '2' experiences three thermal cycles. Therefore, at the end of the deposition process (after depositing layer 4), the hardness decreases with distance from the top of the part. The trend is also observed experimentally (Fig. 8).

Fig. 8 shows that the calculated variation in hardness with the distance from the top of the deposit agrees well with the experimentally measured values [20] for a 10-layer-high thin wall printed

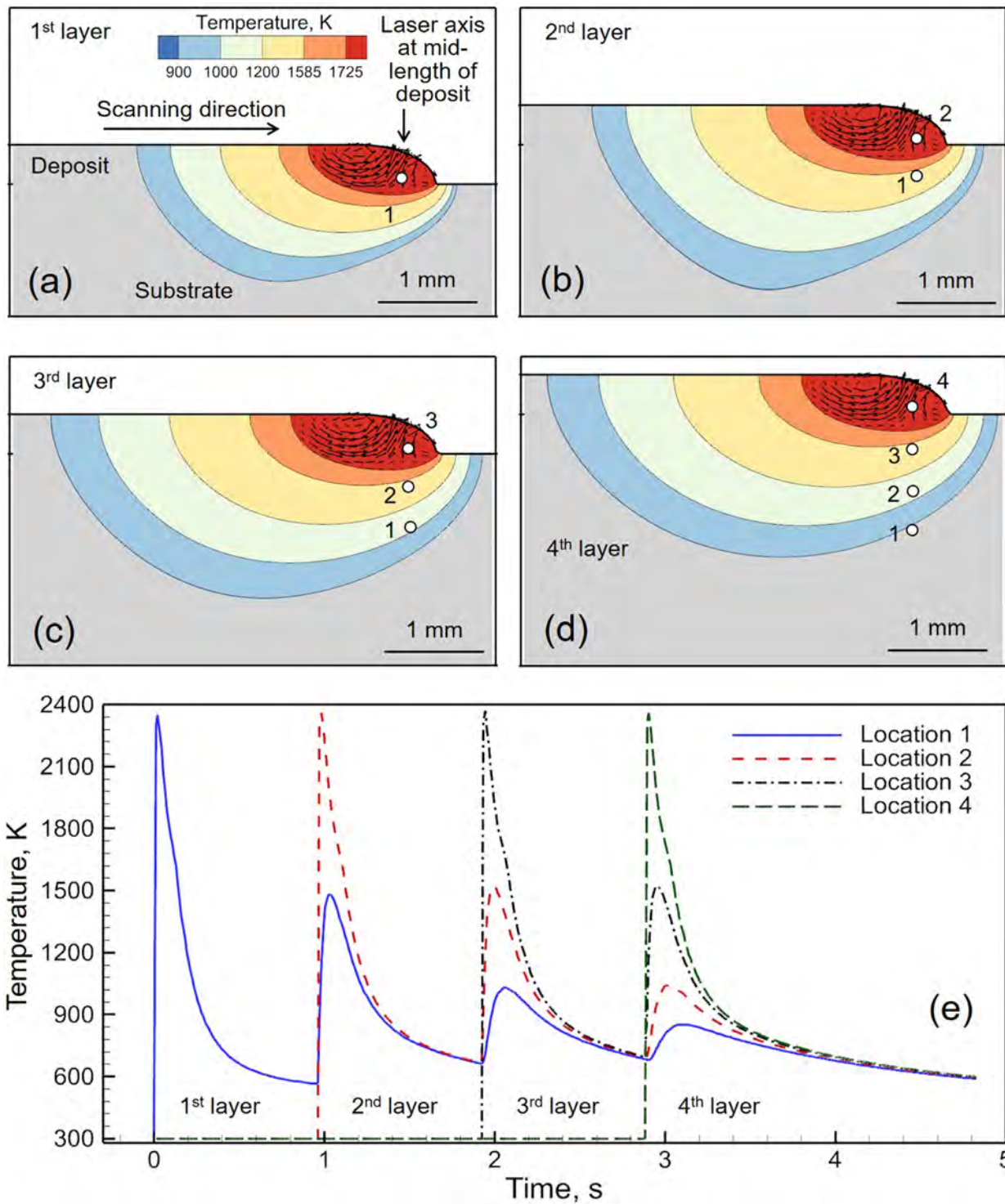


Fig. 6. Computed temperature and velocity fields on longitudinal plane (XZ as shown in Fig. 3) at the mid-width of the deposit during DED-L of H13 tool steel during the deposition of (a) 1st, (b) 2nd, (c) 3rd and (d) 4th layer. The results are for 250 W laser power and 8.47 mm/s scanning speed. Other process parameters are given as set 1 in Table 3. '1', '2', '3' and '4' are four locations at 1st, 2nd, 3rd and 4th layers, respectively as shown in the figures. (e) Thermal cycle calculated at all four locations while depositing the 4 layers.

using gas-atomized powders of H13 tool steel. The hardness was experimentally measured at various heights of the thin wall using a Vickers diamond indenter [20]. Hardness values are calculated at the corresponding locations where measurements were taken. The excellent agreement between the experimental and numerically calculated results indicates that the numerical approach proposed here can be used for the hardness calculations in DED-L

parts with confidence. The two insets in the figure show the corresponding microstructure for two locations. Martensitic microstructure results in a high hardness near the top and tempered martensite reduces the hardness near the bottom. A decrease in hardness with the distance from the top of the deposit is also observed both numerically and experimentally at different scanning speeds (Fig. 9). Good agreements between the calculated and the mea-

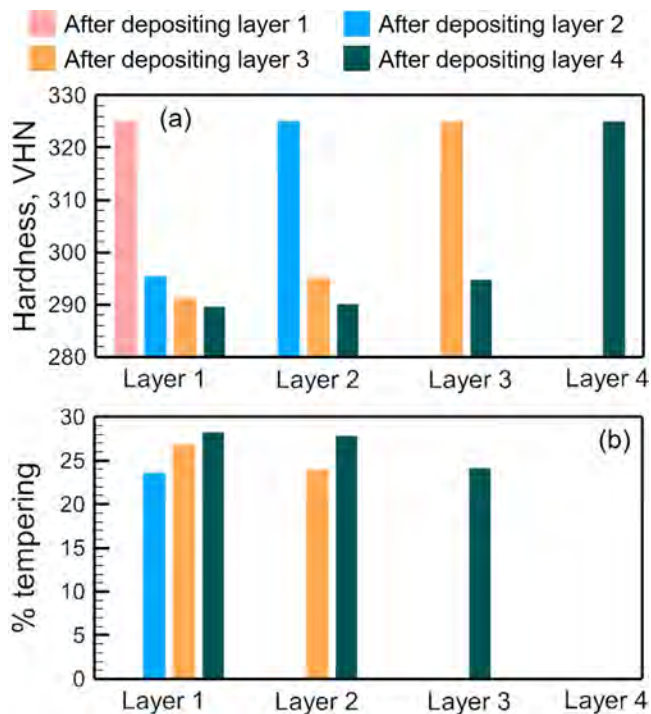


Fig. 7. Calculated variations of (a) hardness and (b) percentage tempering of martensite at 4 layers (calculated at the four locations “1” to “4” shown in Fig. 6) during the depositions of 4 layers. The results are for 250 W laser power and 8.47 mm/s scanning speed. Other process parameters are given as set 1 in Table 3.

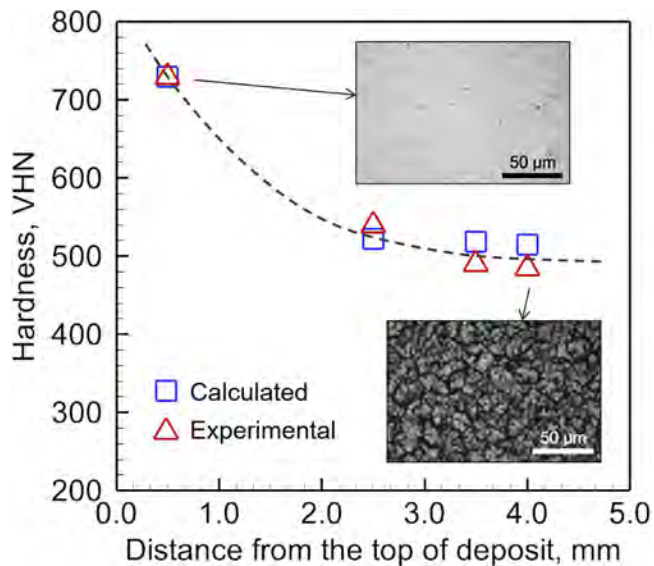


Fig. 8. Comparison between experimentally measured [20] and calculated hardness variations with the distance from the top of the deposit during DED-L of H13 tool steel using the process parameters given as set 3 in Table 3. The results are for a 10 layers high thin wall printed using gas-atomized powders of H13 tool steel. The insets show the corresponding microstructure for two locations. Martensitic microstructure (extremely fine lath martensite at light etching [20]) results in high hardness near the top and tempered martensite (dark etching [20]) reduces the hardness near the bottom.

sured [14] hardness for 9-layer-high thin walls of H13 tool steel fabricated are obtained at two scanning speeds (Fig. 9). A small difference between the calculated and the measured results is perhaps due to both the uncertainties in the hardness measurements and the several simplifying assumptions in modeling to make the numerical calculations tractable. For example, re-austenization due

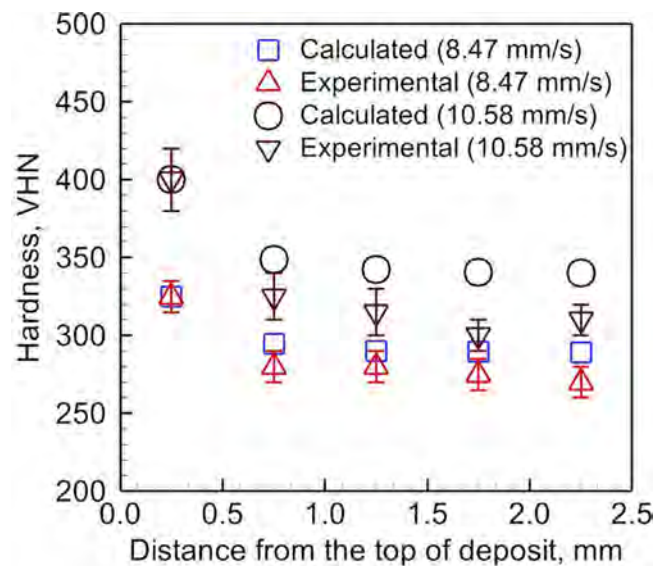


Fig. 9. Comparison between experimentally measured [14] and calculated hardness variations with the distance from the top of the deposit during DED-L of H13 tool steel using the process parameters given as set 1 in Table 3. For all cases laser power is 250 W. Multiple measurements are taken several times at the same height and an average value of hardness is reported. Error bars show the measurement error in hardness.

to reheating of martensite has been ignored for the following reasons. The formation of austenite from martensite is a diffusion controlled, relatively slow process and the time available for the reheating of martensite to form austenite is very short, often fraction of a second. The re-austenization of martensite may happen only during the deposition of the next layer where the temperature may exceed the austenizing temperature for a very short time, and the volume fraction of re-formed austenite is evidently small enough to ignore. In contrast, tempering of martensite takes place for the entire duration of the deposition of all layers. Most importantly, the trends in the computed hardness variation match fairly

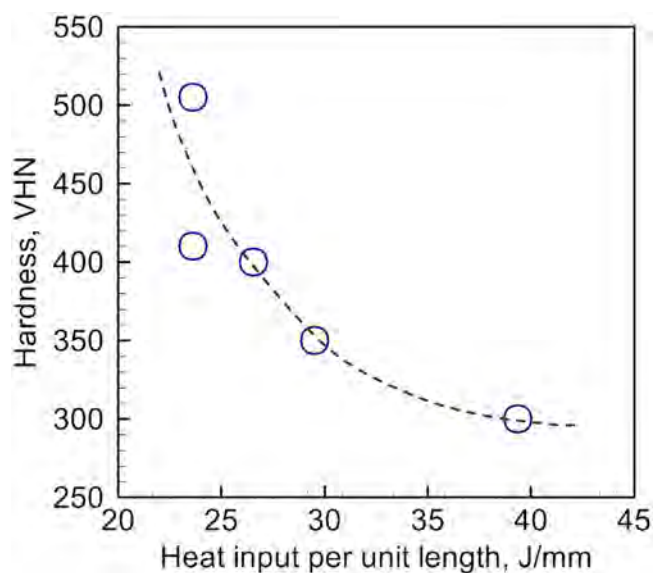


Fig. 10. Variation of hardness with heat input per unit length of the deposit (laser power / scanning speed). The plot is based on the experimental data for DED-L of H13 tool steel adapted from the literature [14]. Other process parameters are given as set 1 in Table 3. The hardness values are measured at the top of the part containing martensite which does not experience any further heating and cooling.

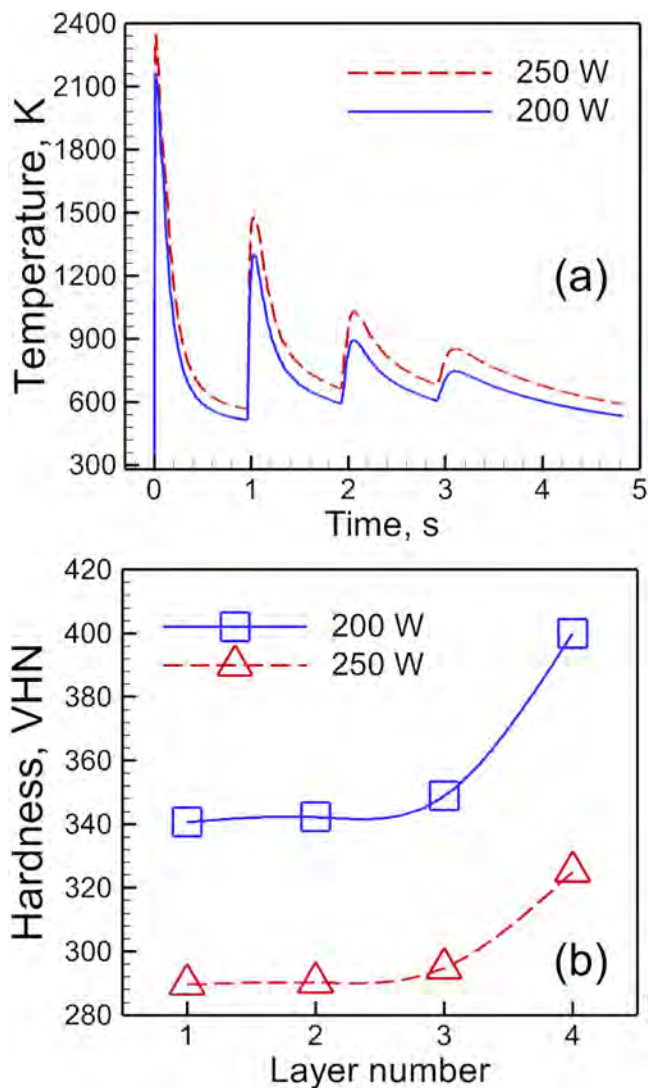


Fig. 11. (a) Calculated thermal cycles at the 1st layer (on top surface at mid-length and mid-width of the track) during deposition of 4 layers at different laser powers. (b) Calculated hardness at 4 layers after the deposition process for two laser powers. Hardness values are calculated on the top at the mid-length and mid-width of each layer. The results are for DED-L of H13 tool steel using scanning speed of 8.47 mm/s and other process parameters are given as set 1 in Table 3.

well with the experimental observations when re-austenization is ignored and neglecting re-austenitization makes the calculations tractable with no apparent loss of accuracy. Fig. 9 shows that slower scanning which results in higher heat input, reduces hardness as explained below.

Fig. 10 shows that a component built using a low heat input per unit length (laser power/scanning speed) exhibits a high hardness [14]. Low heat input results in a rapid cooling which forms more martensite and makes the component harder. Variation in laser power which controls the heat input also affects the hardness (Fig. 11). First, a high laser power increases the heat input and decreases the cooling rate which as a result reduces the hardness as shown in Fig. 11(b). In addition, a higher laser power increases the temperature as shown in Fig. 11(a). A higher temperature results in a more pronounced reheating of the previously deposited layers which transforms more martensite into tempered martensite and reduces hardness. Therefore, hardness decreases with an increase in laser power at all four layers as shown in Fig. 11(b).

4. Summary and conclusion

A property prediction model which is a combination of a heat transfer and fluid flow model of DED-L and a Johnson-Mehl-Avrami (JMA) based kinetic model is used to predict hardness in H13 tool steel components. The thermal cycles at several locations in the component, computed from the heat transfer and fluid flow model, are tested using independent experimental results. Isothermal aging data of H13 tool steel are used to estimate the constants of JMA equation. The JMA equation is integrated over the calculated thermal cycle to predict the hardness. Calculated hardness values match well with independent experimental data. Below are the specific findings.

- (1) The hardness of H13 tool steel is correctly predicted as a function of process variables using a heat transfer and fluid flow model, a model for phase transformation kinetics and tempering data.
- (2) The hardness of a location in the component continues to decrease with the intensity, duration and the number of repeated thermal cycles. Martensite that forms due to high cooling rates in DED-L subsequently decomposes into tempered martensite because of tempering that involves multiple thermal cycles. As a result, hardness of the component decreases.
- (3) Lower layers of a component experience a greater number of thermal cycles during the deposition of subsequent layers and exhibit lower hardness due to tempering. Therefore, hardness decreases with the distance from the top of the deposit.
- (4) High heat input due to high laser power and slow scanning speed results in low cooling rate and decreased hardness. In addition, high heat input increases the temperature at a given location and forms tempered martensite. Due to both these reasons, components made with higher heat input exhibit lower hardness.

The quantitative approach used here can also be expanded for predicting hardness in other commercial alloys, such as precipitation hardened nickel base superalloys, at least in principle. However, because of the complexity of aging of such alloys, calculation of hardness is not straightforward. More work is needed to develop aging kinetics of these alloys before they can be integrated with the computed thermal cycles. [42,43]. Similar hardness can be obtained in a part consisting of different combinations of microstructures. It is not straightforward to calculate hardness by capturing the effects of all possible phases and thus is left as a future work. Since the spatial and temporal variation of hardness (strength) can be predicted as a function of process variables, control of microstructure and properties are within reach of the materials research community, at least for relatively simple alloys.

Declaration of Competing Interest

None.

Acknowledgements

This research is being performed using funding received from the DOE Office of Nuclear Energy's Nuclear Energy Enabling Technologies Program, as part of project 19-17206 of the Advanced Methods for Manufacturing Program.

Appendix : Solid state phase transformation of martensite to tempered martensite

H13 tool steel is a martensitic steel which forms martensite at a very low cooling rate of 0.1°C/s as evident from the CCT dia-

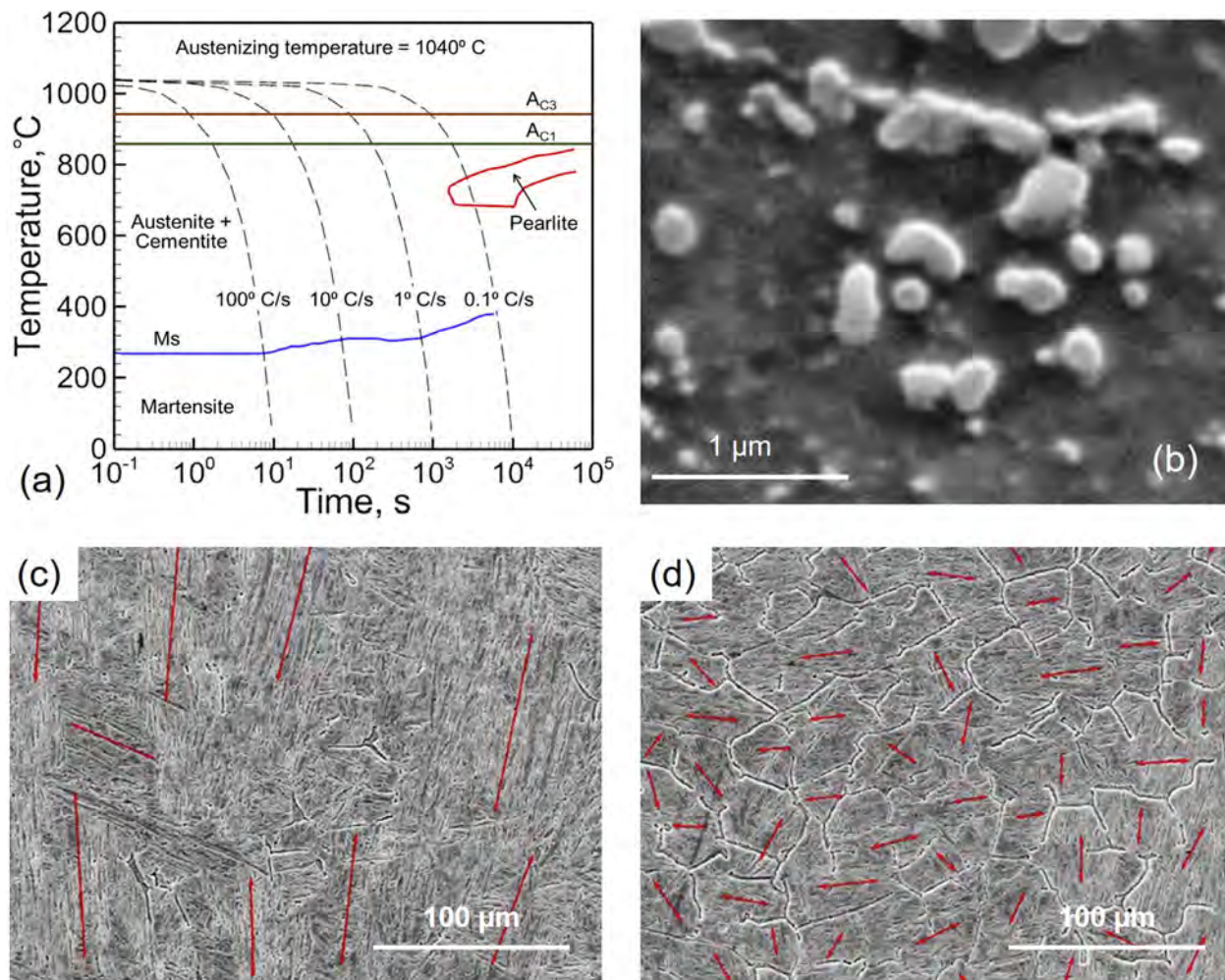


Fig. A1. (a) Continuous cooling transformation (CCT) diagram of H13 tool steel. Adapted from [18]. (b) Formation of chromium and vanadium rich carbides in the tempered martensitic microstructure during additive manufacturing of H13 tool steel [44]. Formation of (c) martensitic structure in the as-deposited part and (d) tempered martensitic structure with carbide precipitates after the part experiences reheating and cooling during the deposition of subsequent layer [23].

gram (Fig. A1(a)). In directed energy deposition of H13 tool steel, the cooling rates are significantly higher than this critical cooling rate of martensite formation. Therefore, additive manufactured H13 tool steel components are known to exhibit martensitic microstructure. However, the extent of formation of martensite depends on the martensite start (M_s in Fig. A1(a)) and finish temperatures both of which may vary depending on the austenizing temperature (Fig. A1(a)). If the lowest temperature in a thermal cycle during cooling is above the martensite start temperature, no martensite forms. In contrast, 100% martensite forms when the lowest temperature is below martensite finish temperature. However, for H13 tool steel, often the martensite finish temperature is below the room temperature. For most of the cases of additive manufacturing of H13 tool steel, the lowest temperature of the thermal cycle is between the martensite start and finish temperatures indicating a presence of metastable austenite along with martensite. The martensitic microstructure is reheated and cooled during the deposition of subsequent layers resulting in transformation of the martensite to tempered martensite. Tempered martensitic microstructure consists of fine carbides ($\sim 1 \mu\text{m}$ in size) of chromium and vanadium (Fig. A1(b)) which significantly affect the hardness. Martensite laths (Fig. A1(c)) can be observed in the as-deposited layers during additive manufacturing of H13 tool steel. The tempered martensitic structure (Fig. A1(d)) due to reheating and cooling because of deposition of multiple layers shows carbide

precipitates along the grain boundary. The extent of transformation of martensite into tempered martensite depends on the temperature variation which is significantly affected by the processing conditions used in additive manufacturing.

References

- [1] T. DebRoy, H.L. Wei, J.S. Zuback, T. Mukherjee, J.W. Elmer, J.O. Milewski, A.M. Beese, A. Wilson-Heid, A. De, W. Zhang, Additive manufacturing of metallic components – Process, structure and properties, *Prog. Mater. Sci.* 92 (2018) 112–224.
- [2] T. DebRoy, T. Mukherjee, H.L. Wei, J.W. Elmer, J.O. Milewski, Metallurgy, mechanistic models and machine learning in metal printing, *Nat. Rev. Mater.* (2020), doi:10.1038/s41578-020-00236-1.
- [3] T. DebRoy, T. Mukherjee, J.O. Milewski, J.W. Elmer, B. Ribic, J.J. Blecher, W. Zhang, Scientific, technological and economic issues in metal printing and their solutions, *Nat. Mater.* 18 (2019) 1026–1032.
- [4] H.L. Wei, T. Mukherjee, W. Zhang, J.S. Zuback, G.L. Knapp, A. De, T. DebRoy, Mechanistic models for additive manufacturing of metallic components, *Prog. Mater. Sci.* (2020), doi:10.1016/j.pmatsci.2020.100703.
- [5] G.L. Knapp, T. Mukherjee, J.S. Zuback, H.L. Wei, T.A. Palmer, A. De, T. DebRoy, Building blocks for a digital twin of additive manufacturing, *Acta Mater* 135 (2017) 390–399.
- [6] D. Herzog, V. Seyda, E. Wycisk, C. Emmelmann, Additive manufacturing of metals, *Acta Mater* 117 (2016) 371–392.
- [7] Z. Xia, J. Xu, J. Shi, T. Shi, C. Sun, D. Qiu, Microstructure evolution and mechanical properties of reduced activation steel manufactured through laser directed energy deposition, *Add. Manufact.* 33 (2020) 101114.
- [8] N.T. Aboulkhair, M. Simonelli, L. Parry, I. Ashcroft, C. Tuck, R. Hague, 3D printing of Aluminium alloys: additive Manufacturing of Aluminium alloys using selective laser melting, *Prog. Mater. Sci.* 106 (2019) 100578.

- [9] J.P. Oliveira, T.G. Santos, R.M. Miranda, Revisiting fundamental welding concepts to improve additive manufacturing: from theory to practice, *Prog. Mater. Sci.* 107 (2020) 100590.
- [10] D.D. Gu, W. Meiners, K. Wissenbach, R. Poprawe, Laser additive manufacturing of metallic components: materials, processes and mechanisms, *Int. Mater. Rev.* 57 (3) (2012) 133–164.
- [11] J.A. Koepf, M.R. Gotterbarm, M. Markl, C. Körner, 3D multi-layer grain structure simulation of powder bed fusion additive manufacturing, *Acta Mater* 152 (2018) 119–126.
- [12] G.P. Dinda, A.K. Dasgupta, J. Mazumder, Texture control during laser deposition of nickel-based superalloy, *Scripta Mater* 67 (5) (2012) 503–506.
- [13] J.W. Elmer, T.A. Palmer, W. Zhang, T. DebRoy, Time resolved X-ray diffraction observations of phase transformations in transient arc welds, *Sci. Technol. Weld. Join.* 13 (3) (2008) 265–277.
- [14] V.D. Manvatkar, A.A. Gokhale, G.J. Reddy, U. Savitha, A. De, Investigation on laser engineered net shaping of multilayered structures in H13 tool steel, *J Laser Appl* 27 (3) (2015) 032010.
- [15] D.P. Karmakar, M. Gopinath, A.K. Nath, Effect of tempering on laser remelted AISI H13 tool steel, *Surf. Coat. Technol.* 361 (2019) 136–149.
- [16] N.S. Bailey, C. Katinas, Y.C. Shin, Laser direct deposition of AISI H13 tool steel powder with numerical modeling of solid phase transformation, hardness, and residual stresses, *J Mater. Process. Technol.* 247 (2017) 223–233.
- [17] V.D. Manvatkar, A. De, A.A. Gokhale, G.J. Reddy, An Integrated Approach towards Estimation of Build Profile and Mechanical Properties in LENS® Deposit of H13 Tool Steel, *Mater. Sci. Technol. (MS&T)* (2011) Columbus, Ohio.
- [18] J. Džugan, K. Halmešová, M. Ackermann, M. Koukolikova, Z. Trojanová, Thermo-physical properties investigation in relation to deposition orientation for SLM deposited H13 steel, *Thermochim. Acta* 683 (2020) 178479.
- [19] G. Telasang, J. Dutta Majumdar, N. Wasekar, G. Padmanabham, I. Manna, Microstructure and mechanical properties of laser clad and post-cladding tempered AISI H13 tool steel, *Metal. Mater. Trans. A* 46 (5) (2015) 2309–2321.
- [20] A.J. Pinkerton, L. Li, Direct additive laser manufacturing using gas-and water-atomised H13 tool steel powders, *Int. J Adv. Manufact. Technol.* 25 (5–6) (2005) 471–479.
- [21] J. Zhu, G.T. Lin, Z.H. Zhang, J.X. Xie, The martensitic crystallography and strengthening mechanisms of ultra-high strength rare earth H13 steel, *Mater. Sci. Eng. A* 797 (2020) 140139.
- [22] Y. Ali, P. Henckell, J. Hildebrand, J. Reimann, J.P. Bergmann, S. Barnikol-Oettler, Wire arc additive manufacturing of hot work tool steel with CMT process, *J Mater. Process. Technol.* 269 (2019) 109–116.
- [23] J. Ge, T. Ma, Y. Chen, T. Jin, H. Fu, R. Xiao, Y. Lei, J. Lin, Wire-arc additive manufacturing H13 part: 3D pore distribution, microstructural evolution, and mechanical performances, *J Alloy. Comp.* 783 (2019) 145–155.
- [24] Y.X. Wu, W.W. Sun, X. Gao, M.J. Styles, A. Arlazarov, C.R. Hutchinson, The effect of alloying elements on cementite coarsening during martensite tempering, *Acta Mater* 183 (2020) 418–437.
- [25] E.I. Galindo-Nava, P.E.J. Rivera-Díaz-del-Castillo, A model for the microstructure behaviour and strength evolution in lath martensite, *Acta Mater* 98 (2015) 81–93.
- [26] L.R.C. Malheiros, E.A.P. Rodriguez, A. Arlazarov, Mechanical behavior of tempered martensite: characterization and modeling, *Mater. Sci. Eng. A* 706 (2017) 38–47.
- [27] E. Biro, J.R. McDermid, S. Vignier, Y.N. Zhou, Decoupling of the softening processes during rapid tempering of a martensitic steel, *Mater. Sci. Eng. A* 615 (2014) 395–404.
- [28] Y.L. Sun, G. Obasi, C.J. Hamelin, A.N. Vasileiou, T.F. Flint, J.A. Francis, M.C. Smith, Characterisation and modelling of tempering during multi-pass welding, *J Mater. Process. Technol.* 270 (2019) 118–131.
- [29] Q. Zhang, J. Xie, Z. Gao, T. London, D. Griffiths, V. Oancea, A metallurgical phase transformation framework applied to SLM additive manufacturing processes, *Mater. Des.* 166 (2019) 107618.
- [30] A. Kumar, S. Mishra, T. DebRoy, J.W. Elmer, Optimization of the Johnson-Mehl-Avrami equation parameters for α -ferrite to γ -austenite transformation in steel welds using a genetic algorithm, *Metal. Mater. Trans. A* 36 (1) (2005) 15–22.
- [31] J. Brooks, C. Robino, T. Headley, S. Goods, M. Griffith, Microstructure and Property Optimization of LENS Deposited H13 Tool Steel, *Int. Solid Freeform Fab. Symp.* (1999).
- [32] V. Manvatkar, A. De, T. DebRoy, Heat transfer and material flow during laser assisted multi-layer additive manufacturing, *J Appl. Phys.* 116 (12) (2014) 124905.
- [33] V. Manvatkar, A. De, T. DebRoy, Spatial variation of melt pool geometry, peak temperature and solidification parameters during laser assisted additive manufacturing process, *Mater. Sci. Technol.* 31 (2015) 924–930.
- [34] S. Oh, H. Ki, Prediction of hardness and deformation using a 3-D thermal analysis in laser hardening of AISI H13 tool steel, *Appl. Thermal Eng.* 121 (2017) 951–962.
- [35] P. Farahmand, P. Balu, F. Kong, R. Kovacevic, Investigation of thermal cycle and hardness distribution in the laser cladding of AISI H13 tool steel produced by a high power direct diode laser, *ASME Int. Mech. Eng. Cong. Expo.* (2013) 56185.
- [36] H.L. Wei, G.L. Knapp, T. Mukherjee, T. DebRoy, Three-dimensional grain growth during multi-layer printing of a nickel-based alloy Inconel 718, *Add. Manufact.* 25 (2019) 448–459.
- [37] S. Pogatscher, H. Antrekowitsch, H. Leitner, T. Ebner, P.J. Uggowitzer, Mechanisms Controlling the Artificial Aging of Al-Mg-Si Alloys, *Acta Mater* 59 (2011) 3352–3363.
- [38] S. Esmaili, D.J. Lloyd, W.J. Poole, Modeling of Precipitation Hardening for the Naturally Aged Al-Mg-Si-Cu Alloy AA6111, *Acta Mater* 51 (2003) 3467–3481.
- [39] W. Ou, T. Mukherjee, G.L. Knapp, Y. Wei, T. DebRoy, Fusion zone geometries, cooling rates and solidification parameters during wire arc additive manufacturing, *Int. J Heat Mass Trans.* 127 (2018) 1084–1094.
- [40] A.P. Sekhar, S. Nandy, K.K. Ray, D. Das, Prediction of Aging Kinetics and Yield Strength of 6063 Alloy, *J Mater. Eng. Perform.* 28 (5) (2019) 2764–2778.
- [41] S. Ghosh, J. Choi, Modeling and experimental verification of transient/residual stresses and microstructure formation in multi-layer laser aided DMD process, *J Heat Trans* 128 (2006) 662–679.
- [42] P. Nie, O.A. Ojo, Z. Li, Numerical modeling of microstructure evolution during laser additive manufacturing of a nickel-based superalloy, *Acta Mater* 77 (2014) 85–95.
- [43] K.N. Amato, S.M. Gaytan, L.E. Murr, E. Martinez, P.W. Shindo, J. Hernandez, S. Collins, F. Medina, Microstructures and mechanical behavior of Inconel 718 fabricated by selective laser melting, *Acta Mater* 60 (5) (2012) 2229–2239.
- [44] D. Cormier, O. Harrysson, H. West, Characterization of H13 steel produced via electron beam melting, *Rapid Prototyp. J.* 10 (1) (2004) 35–41.